Time-and space-resolved nonlinear magnetoacoustic dynamics

M. Kraimia, P. Kuszewski, J.-y Duquesne, A. Lemaitre, F. Margaillan, C. Gourdon, L. Thevenard

Time- and space-resolved nonlinear magnetoacoustic dynamics

M. Kraimia,[1,2] P. Kuszewski,[1] J.-Y. Duquesne,[1] A. Lemaître,[3] F. Margaillan,[1] C. Gourdon,[1] and L. Thevenard[1,*]

[1]*Sorbonne Université, CNRS, Institut des Nanosciences de Paris, 4 place Jussieu, 75005 Paris, France*

[2]*Faculté des Sciences de Bizerte, LR01ES15 Laboratoire de Physique des Matériaux: Structure et Propriétés, Université de Carthage, 7021 Zarzouna, Bizerte, Tunisia*

[3]*Centre de Nanosciences et de Nanotechnologies, CNRS, Université Paris-Sud, Université Paris-Saclay, 91120 Palaiseau, France*

(Received 14 February 2020; accepted 25 March 2020; published 20 April 2020)

Nonlinear magnetization dynamics are of great interest, being, for instance, leveraged for neuromorphic computing in spin-transfer torque nano-oscillators. Here, we demonstrate how to implement magnetoacoustics to reach this regime, using monochromatic ($f_{saw} = 450$ MHz) surface acoustic waves traveling on a thin layer of (Ga,Mn)As. By careful tuning of the precession frequency to both f_{saw} and $2f_{saw}$ using the magnetic field and temperature, we evidence clear signatures of a nonlinear magnetoacoustic response of the magnetic dynamics using the time- and space-resolved Kerr effect: (i) frequency and wave-vector doubling in time and space, respectively, (ii) quadratic (sublinear) evolution of the precession amplitude at $2f_{saw}$ (f_{saw}) with acoustic amplitude, and (iii) resonance field shift. While (i) can be well reproduced by a parametric resonance model where nonlinearities arise solely from the SAW, we show that features (ii) and (iii) also involve intrinsic magnetic nonlinearities. Understanding the conditions leading to these nonlinearities will mean better control of the acoustic-wave-driven magnetization dynamics, in order to implement optimally the wave properties enabled by this approach.

DOI: 10.1103/PhysRevB.101.144425

I. INTRODUCTION

The nonlinearity of the Landau-Lifshitz-Gilbert (LLG) equation governing magnetization dynamics makes it relatively easy to evidence nonlinear behavior in magnetic systems, such as frequency mixing or parametric pumping, i.e., the appearance of multiples or fractions of the eigenfrequency ($2\omega_0$, $3\omega_0$, $\omega_0/2$, ...) [1–3]. These effects are of great technological interest, as they are involved in precessional switching [4,5], the response of spin-transfer torque nano-oscillators [6], magnetic nanostructure-based neuromorphic computing [7,8], and exciting prototype devices of magnon-based logic [9] such as the magnon transistor [10], or magnonic directional coupler [11].

Magnons (spin waves) are generated inductively by current-driven radio-frequency (rf) magnetic fields but also very efficiently by rf bulk or surface acoustic waves (SAWs). Magnetoelasticity can indeed induce an effective rf field and there have been recent reports of the magnetization dynamics [12–15] and ferromagnetic resonance [16,17] that ensue. Paralleling what has been observed under inductive excitation [18,19], the acoustic parametric pumping of spin waves has been studied, and monitored by the absorption of the acoustic wave [3,20–24]. Looking at the magnetization dynamics, the appearance of $2f_{saw}$ following the excitation of precession by a monochromatic SAW at f_{saw} (frequency doubling) was recently evidenced [12]. However, owing to the hitherto lack of combined space and time resolution in the probing of magnetoacoustic dynamics, open questions remain pertaining to, e.g., the dependence of the spin-wave amplitude and eigenfrequency on the SAW amplitude, or the spatial frequencies and wavefront shape of the dynamics.

Using electrically excited SAWs traveling on a layer of ferromagnetic (Ga,Mn)As and combining space- and time-resolved detection of both the magnetization dynamics and the SAW amplitude, we evidence three different features of nonlinear behavior in a coupled magnetization/strain system: (i) frequency and wave-vector doubling in the magnetization dynamics but not in the SAW, (ii) nonlinearity of the precession amplitude, and (iii) a resonance field shift. Whereas at low SAW amplitudes these results are quantitatively very well accounted for in a perturbative scheme using a parametric oscillator model [12], we show that a full LLG solution is necessary out of this regime. These results validate SAWs, weakly attenuated strain excitations, as a relevant tool to perform remote and agile nonlinear spin-wave manipulation, something up to now forbidden by the local and short-lived spin waves excited inductively [25].

II. EXPERIMENTAL DETAILS

Whereas most magnetoacoustics reports use room-temperature ferro- or ferrimagnets such as iron [26], nickel [12,16], cobalt [27], or YIG [28], we are using the dilute magnetic semiconductor (Ga,Mn)As. It offers a different set of magnetic parameters at all temperatures up to the Curie temperature T_c, and a convenient tuning of magnetoelastic constants by growth [29]. In particular, the frequency of the uniform spin-wave mode can easily be tuned to the acoustic frequency by varying the temperature, in addition to applying a bias magnetic field. Moreover, the magnetoelasticity of

*thevenard@insp.jussieu.fr

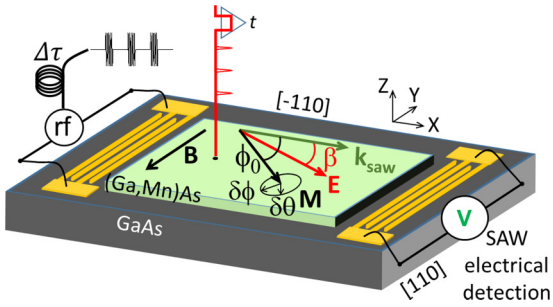

FIG. 1. Schematics of the experimental setup (not to scale). The delay line between the two transducers is 2 mm. Angle and axis definitions: The SAW wave vector $\mathbf{k}_{saw}$ is along [-110], and the static magnetization and incoming probe polarization are indicated by the angles ϕ_0 and β with respect to $\mathbf{k}_{saw}$. $\Delta\tau$ is an electronic delay between the firing of the rf bursts and the probe laser pulses. Their arrival time t is controlled by an optical delay line.

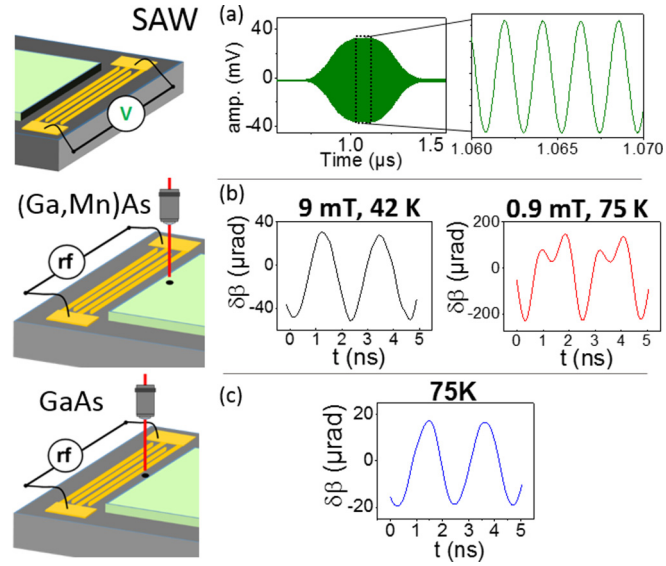

FIG. 2. (a) Acoustic echo recorded electrically on the detection transducer (triggered off the electromagnetic radiation). The amplitude is used for SAW-FMR analysis displayed in Fig. 3. (b) Time scans taken on (Ga,Mn)As at either 9 mT ($T = 42$ K) or 0.9 mT ($T = 75$ K), polarization angle $\beta = 0°$. (c) Time scans taken on GaAs, on the 15-μm gap between the exciting IDT and the (Ga,Mn)As mesa, $\beta = 45°$. For all time scans shown here, $f_{saw} = 452$ MHz and $\Delta\tau$ is chosen to probe the center of the acoustic burst.

(Ga,Mn)As can readily be addressed by the ϵ_{XX}, ϵ_{ZZ}, and ϵ_{XZ} strain components of Rayleigh surface acoustic waves [14,30,31], with X parallel to $\mathbf{k}_{saw}$, the SAW wave vector, and Z denoting the normal to the sample plane (Fig. 1).

Here, the 45-nm-thick (Ga,Mn)As layer is grown by molecular beam epitaxy and annealed for 16 h at 200 °C, at which point the T_c reached 120 K, before being processed for the piezoelectric SAW excitation. For this, a 2×2 mm^2 mesa is wet-etched down to the insulating (001) GaAs substrate in order to evaporate two pairs of interdigitated aluminum transducers (IDTs, 42 nm thick, 1 mm aperture, and 300 μm width). These consist of 25 pairs of split 5:2 electrodes [32], which supplied with an rf voltage burst emit monochromatic 151, 301, 452, or 602 MHz SAWs traveling along the [-110] direction (Fig. 1). The sample exhibits competing biaxial and uniaxial magnetic anisotropies, the latter arising from magnetoelasticity (B_1, B_2 constants, see Appendix A). The resulting easy axis is along [-110] at low temperature. In the following, the field is thus applied along the hard [110] axis to lower the precession frequency up to H_a at which the magnetization aligns with the field. This sample was used in Ref. [14] to evidence the concomitant acoustic and magnetic resonance at these four frequencies. In the present work, we focus on the nonlinear behavior of the system, and reveal the spatial dependency of the magnetization dynamics.

Two types of data are acquired. In SAW ferromagnetic resonance (SAW-FMR) experiments, the SAW is picked up piezoelectrically by the opposite IDT after traveling across the mesa [Fig. 2(a)], and the amplitude of the detected acoustic echo is monitored with respect to the field amplitude. This is readily illustrated by the $T = 42$ K and $T = 75$ K SAW-FMR curves of Figs. 3(a) and 3(b). The former one exhibits a single resonant absorption peak at 26 mT, a field at which the precession frequency f_0 lies closest to the SAW frequency, whereas the latter one exhibits two peaks at 0.5 and 9 mT since the $f_0(B)$ curve crosses f_{saw} twice [Figs. 3(g) and 3(h)].

In time-resolved Kerr effect (TR-MOKE) experiments, 200-fs linearly polarized laser pulses are synchronized to the rf bursts and focused onto the sample using a microscope objective after passing through an optical delay line. The polarization makes an angle β with the [-110] axis of the sample (Fig. 1). The polarization rotation $\delta\beta$ is monitored using a balanced optical detection bridge. A careful analysis of the dependence of $\delta\beta$ on the incoming polarization β yields the out-of-plane $\delta\theta$ and in-plane $\delta\phi$ magnetization dynamics components (Fig. 1), as well as the strain dynamics, via the photoelastic effect (PE). $\delta\theta$ is independent of β, whereas the PE varies as $\epsilon_{XX}(X,t)\sin 2\beta$. Setting the incoming polarization parallel to (45° from) $\mathbf{k}_{saw}$ will thus cancel (maximize) the PE. Finally, time scans (spatial scans) are obtained by scanning the optical delay line (the piezoelectric stage holding the objective). Please refer to Ref. [14] for a more extensive description of the setup and data analysis procedure.

The $\lambda = 721$ nm wavelength and 0.4 numerical aperture objective used yield a spot size of 1.5 μm full width at half maximum (FWHM) so that larger SAW wavelengths will be much better spatially resolved: 151 MHz (and the frequency doubled 302 MHz) corresponds to an 18 μm (9 μm) SAW wavelength while 602 MHz (and the frequency doubled 1.2 GHz) to $\lambda = 4.6$ μm (2.3 μm). Yet higher frequencies will yield a larger signal since the magnetoacoustic resonant absorption increases with f_{saw} [31]. A comfortable compromise for this study has been to use $f_{saw} = 452$ MHz. SAWs were thus excited using 400-ns-long, +28-dBm, 452-MHz bursts at a 252 kHz repetition rate (unless specified). Note that this rate in combination with a 10% duty cycle leads to a substantial stationary heating (see details in Appendix B), so that all the temperatures mentioned in this paper are not *effective* sample temperatures, but rather the temperature at which the cryostat was regulated. These were the conditions used for the 42 and 75 K SAW-FMR curves described above [Figs. 3(a) and 3(b)].

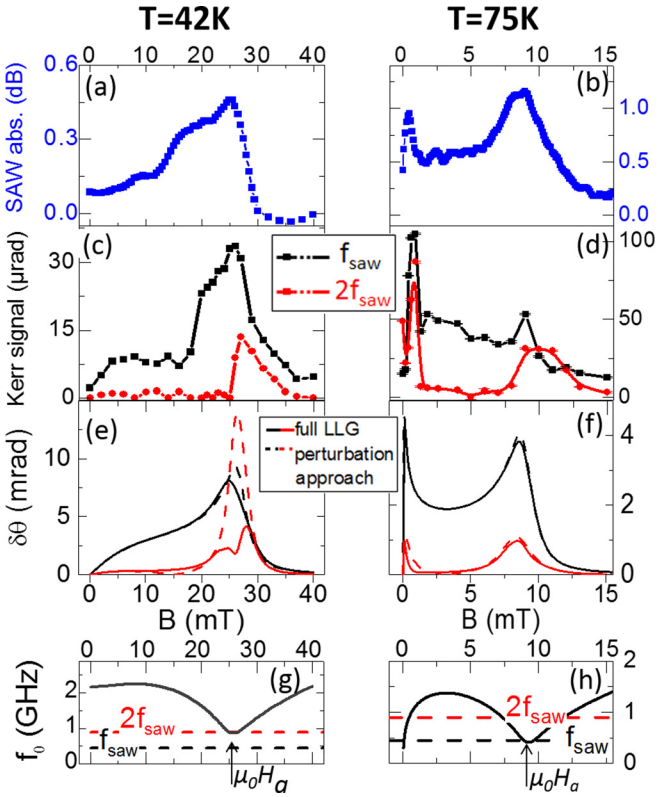

FIG. 3. At two temperatures ($T = 42$ and 75 K): (a), (b) SAW-FMR absorption curve; (c), (d) Kerr signal proportional to the out-of-plane magnetization precession component $\mathcal{K}_\theta = K\delta\theta$; and (e), (f) calculated amplitudes of the out-of-plane component $\delta\theta$ at f_{saw} (black) and $2f_{saw}$ (red). Calculations were done using either a full numerical approach (solid lines) or a perturbative approach (dashed lines) (see text and Appendix A for details). (g), (h) Field dependence of the precession frequency estimated from FMR-determined magnetic anisotropy constants [31] (see Appendix A). At $\mu_0 H_a$, the magnetization aligns with the field.

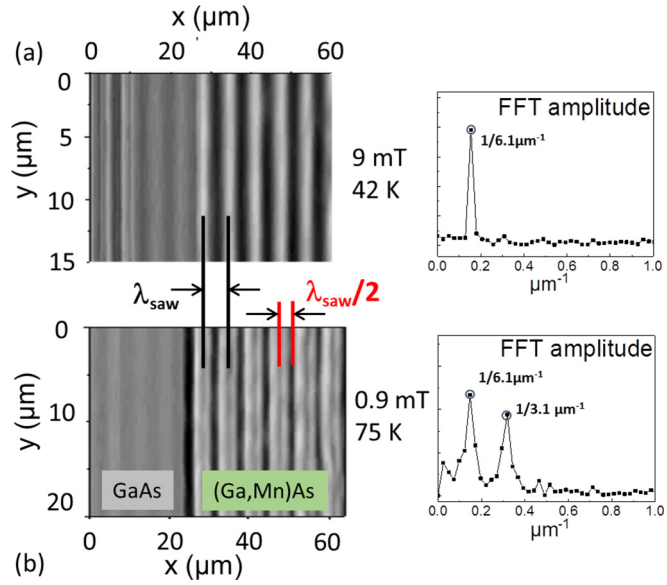

FIG. 4. Spatial scans of the MOKE signal taken close to the exciting IDT over an area overlapping GaAs and (Ga,Mn)As with $\beta = 0°$ and $\Delta\tau$ chosen to probe the magnetization dynamics at the center of the acoustic burst. Associated two-dimensional (2D) fast Fourier transform (FFT) of the (Ga,Mn)As part. (a) Under $B = 9$ mT, $T = 42$ K. (b) Under $B = 0.9$ mT, $T = 75$ K.

III. EVIDENCE OF NONLINEARITIES

A. Frequency doubling

We now turn to the TR-MOKE data. Placing the laser spot on the (Ga,Mn)As about 30 μm from the last tooth of the exciting IDT, and scanning the optical delay line, we see periodic oscillations of the polarization rotation [Fig. 2(b)], i.e., of the magnetization dynamics, since the polarization is aligned with $\mathbf{k}_{saw}$ ($\beta = 0°$). For some fields/temperature the sole frequency content is f_{saw} while for others there is a clear coexistence of f_{saw} and $2f_{saw}$. This is illustrated by comparing the two time scans shown in Fig. 2(b), taken at $B = 9$ mT, $T = 42$ K, and $B = 0.9$ mT, $T = 75$ K. Note that the typical voltage levels arriving on the detection bridge were less than 1 V, and well within the linearity range of the photodiodes. Finally, in conditions of optimized focusing and high acoustic powers, we could also pick up a small but finite $3f_{saw}$ contribution to the time-domain signal.

Keeping the delay line position fixed, one can then raster the objective *spatially*. The resulting maps displayed in Fig. 4 show a spatially oscillating magnetic signal on the (Ga,Mn)As, and much fainter oscillations on the GaAs/IDT part since the photoelastic effect is very weak for $\beta = 0°$. Under $B = 9$ mT, $T = 42$ K, a single spatial frequency is observed, corresponding to $\lambda_{saw} = 6.1$ μm [Fig. 4(a)]. The wavefront is very straight, as expected since the IDT excites a quasi plane wave, and the laser spot is sufficiently far from the edges of the IDT to avoid diffraction. Detecting at the opposite IDT, 2 mm away, evidenced an identically straight magnetic wavefront (not shown) [33]. Under $B = 0.9$ mT, $T = 75$ K [Fig. 4(b)], two wavelengths are observed: λ_{saw} and $\lambda_{saw}/2$ corresponding to $\mathbf{k}_{saw}$ and $2\mathbf{k}_{saw}$. The wavefront is now very slightly corrugated, with minute variations of the relative proportion of λ_{saw} and $\lambda_{saw}/2$ signal amplitudes along the Y axis. This may result from the dispersion of magnetic anisotropy parameters, revealed by the nonlinear magnetization precession. A similar observation had been made when simulating SAW-driven precessional switching, in which nonlinearities are even more pronounced [see Fig. 8(b) of Ref. [31], for instance]. As a first conclusion, clear frequency and wave-vector doubling can be observed in the magnetization dynamics. An analysis of the complete field dependence of the precession amplitudes will be shown in Sec. III C.

B. Quadratic amplitude behavior

To study the dependency of the signal amplitude versus drive (SAW) amplitude, we use to our advantage the fairly long rise time of the acoustic burst [Fig. 2(a)], which is directly related to the width of the transducer (300 μm). For this we record numerous time scans, varying the electronic delay between rf bursts and laser pulses ($\Delta\tau$) to vary the amplitude of the strain arriving under the spot. The laser is first positioned on the (Ga,Mn)As, choosing conditions

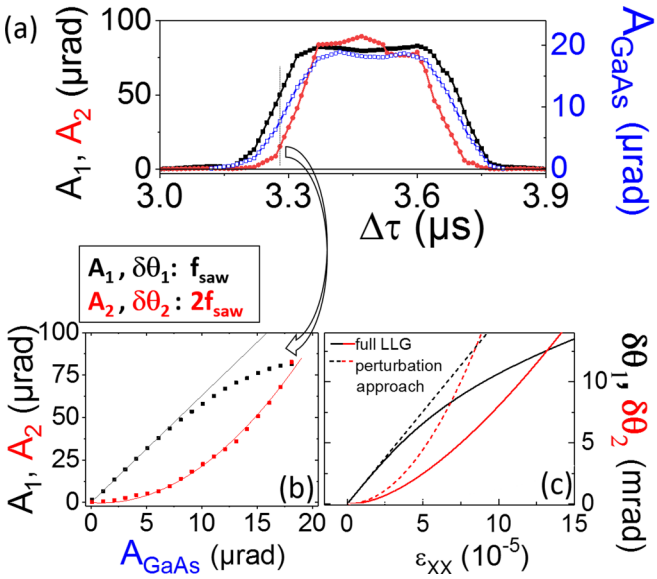

FIG. 5. Study of f_{saw} and $2f_{saw}$ precession amplitudes vs acoustic drive. (a) Experimental amplitude of the polarization rotation on (Ga,Mn)As (A_1 and A_2 at f_{saw} and $2f_{saw}$, respectively) and on GaAs (A_{GaAs} at f_{saw}), at $T = 75$ K, and $B = 0.8$ mT. The laser polarization is $\beta = 0°$ on (Ga,Mn)As and $\beta = 45°$ on GaAs. (b) A_1, A_2 amplitudes plotted vs A_{GaAs} which is proportional to the SAW amplitude. Lines are linear or quadratic fits to the data. (c) Calculation of out-of-plane dynamic magnetization components $\delta\theta_1$, at f_{saw}, and $\delta\theta_2$ at $2f_{saw}$, using either a fully numerical nonapproximated approach (solid lines), or the small-angle perturbation approach (dotted lines) ($B = 0.2$ mT).

yielding frequency doubling ($T = 75$ K, $B = 0.8$ mT), then 15 μm closer to the IDT, on the GaAs [see the corresponding positions in Figs. 2(b) and 2(c)]. On (Ga,Mn)As, the PE contribution is again minimized by taking $\beta = 0°$, so that the polarization rotation mainly reflects the in-plane $\delta\phi$ and out-of-plane $\delta\theta$ magnetization dynamics. The PE contribution is maximized on GaAs by taking $\beta = 45°$, so that $\delta\beta(t)$ is then essentially proportional to the SAW amplitude (ϵ_{XX} component). The resulting time scans are fitted by a function of the form $A_0 + A_1\cos(2\pi f_{saw}t + \phi_1) + A_2\cos(4\pi f_{saw}t + \phi_2)$, where we rely on the fact that the scanning window is much shorter than the 200-ns rise time of the burst.

Only one component at f_{saw} (A_{GaAs}) was necessary to fit the GaAs data, showing that any nonlinearities arising are of magnetic—not acoustic—origin. The A_1, A_2, A_{GaAs} amplitudes are represented versus electronic delay in Fig. 5(a). The overall shape perfectly reflects the envelope of the acoustic echo shape shown in Fig. 2(a). We then plot the A_1, A_2 amplitudes of the rising/falling edges of the burst versus the A_{GaAs} corresponding to the same $\Delta\tau$ delay—legitimate since the (Ga,Mn)As and GaAs data were taken 15 μm apart, equivalent to a mere 5 ns lag of the SAW.

The final curves [Fig. 5(b)] show several very interesting features: The $2f_{saw}$ component has a clear quadratic behavior with the SAW amplitude. Importantly, there seems to be no threshold for the appearance of this double frequency, contrary to the case of parametric pumping [7,34]. The f_{saw} component initially varies linearly with the SAW amplitude, as expected. It then progressively becomes sublinear. This deflation of the $(f_{saw}, \mathbf{k}_{saw})$ mode is a clear signature of nonlinear interactions with higher-order spin-wave modes as will be discussed further on. Note that this was also observed for magnetization dynamics triggered more traditionally by an external rf field [18,19], but without reaching the sublinear regime for the first mode. We thus conclude on a second important feature of this coupled system: the quadratic amplitude variation of the frequency-doubled precessing component.

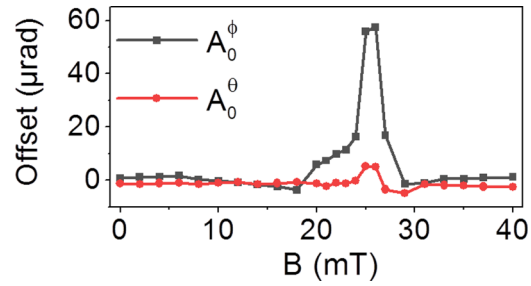

FIG. 6. Offsets of the out-of-plane (A_0^θ) and in-plane (A_0^ϕ) magnetization dynamics components, $T = 42$ K.

C. Magnetoacoustic resonance

We then study more systematically the field dependence of the f_{saw} and $2f_{saw}$ precession amplitudes, choosing the electronic delay $\Delta\tau$ to probe the stationary part of the acoustic burst. For each field, time scans are recorded for six different incoming polarizations ($\beta = 0°$, 30°, 60°, 90°, 120°, and 150°), in order to isolate the β-independent Kerr and $\cos 2\beta$-dependent Voigt amplitudes, varying respectively as $\mathcal{K}_\theta = K\delta\theta(B,t)$, $\mathcal{V}_\phi = 2V\delta\phi(B,t)\cos 2\phi_0(B)$, as explained in detail in Ref. [14]. Note that $\phi_0(B)$ is the static magnetization position, counted with respect to $\mathbf{k}_{saw}$ (see schematics in Fig. 1). Finally, $\mathcal{K}_\theta$ and $\mathcal{V}_\phi$ are fitted as above with $A_0^{\theta,\phi} + A_1^{\theta,\phi}\cos(2\pi f_{saw}t + \phi_1^{\theta,\phi}) + A_2^{\theta,\phi}\cos(4\pi f_{saw}t + \phi_2^{\theta,\phi})$.

The resulting field dependence of $\mathcal{K}_\theta$ is represented in Figs. 3(c) and 3(d) for $T = 42$ and 75 K. The Gaussian beam averaging of the signal has been deconvolved, with the experimental $\mathcal{K}_\theta^{expt}$ multiplied by 1.08 (1.33) to yield $\mathcal{K}_\theta$ at f_{saw} ($2f_{saw}$). While smaller than the amplitude level at f_{saw}, the double frequency is still reasonably well excited, particularly at 75 K. A similar $2f_{saw}/f_{saw}$ amplitude ratio was observed in the $\mathcal{V}_\phi$ component (not shown). A single (double) resonance was observed at $T = 42$ K ($T = 75$ K), with resonance fields very similar to those of SAW-FMR [Figs. 3(a) and 3(b)]. Note that the position and respective amplitudes of the f_{saw} and $2f_{saw}$ depended acutely on the SAW power and precise temperature.

Using the same set of data, we can also plot the offset components of the $\mathcal{K}\delta\theta$, $\mathcal{V}_\phi$ terms: A_0^θ and A_0^ϕ. This is shown in Fig. 6 for $T = 42$ K ($T = 75$ K data available upon request). Both A_0^θ and A_0^ϕ are negligibly small except close to the resonance, peaking at respectively 5 and 57 μrad. These offsets can be written as $A_0^\theta = \mathcal{K}\delta\theta_0(B)$ and $A_0^\phi = 2\mathcal{V}\cos 2\phi_0\delta\phi_0(B)$. Their existence implies that the position around which the

magnetization precesses undergoes a slight *shift* away from its SAW-free equilibrium position. Since the Voigt coefficient $\mathcal{V}$ is typically five to ten times smaller than the Kerr one $\mathcal{K}$ [35], and $\cos 2\phi_0 < 1$, we can safely state that at resonance $\delta\phi_0 \gg \delta\theta_0$. No offset was observed at temperatures for which only one precession frequency was observed. These offsets are not expected in a linear FMR regime and are a clear marker of nonlinearities. They can be found in a parametric oscillator model (see the next section and Appendix A) since a perturbation at ω_{saw} not only provides oscillations at $\omega_{saw} + \omega_{saw} = 2\omega_{saw}$ but also a constant signal at the difference frequency ($\omega_{saw} - \omega_{saw} = 0$). Offsets also appear concomitantly with the large precession amplitudes that announce the onset of SAW-driven precessional switching [30].

D. Resonance field shift

Since the precession frequency depends on the mean magnetization position, the $\delta\phi_0$ shift should also induce a shift of the resonance field when increasing the driving force, as observed in Refs. [36–38] under rf field excitation. Having convinced ourselves of the equivalence of acoustic and magnetic resonance curves (Fig. 3), and since the former are much quicker to obtain, we check for this resonance field shift by measuring SAW-FMR curves at increasing input rf powers (SAW amplitudes). For this we decrease the rf repetition rate to 7.3 kHz, to be certain that the effective sample temperature remains constant as the input rf power is varied (see Appendix B). The temperature set point is raised to 87 K so that the effective sample temperature lies close to that of the 75 K experiments taken at 252 kHz (Figs. 3–5). Figure 7 shows SAW-FMR curves taken for input powers varying between +10 and +32 dBm. The resonance field remains invariant up to +18 dBm, at which point it starts to downshift, as expected from the above-described nonlinearities. Note that such nonlinear acoustic behavior had already been observed [5,39], but the time-domain nonlinear behavior of the magnetic dynamics had not been simultaneously probed.

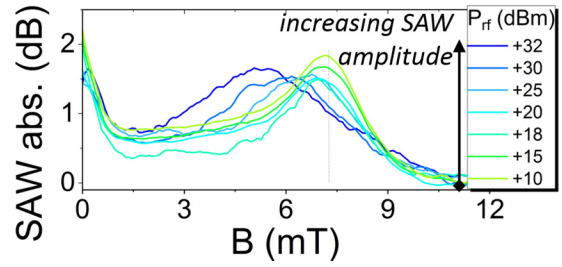

FIG. 7. SAW-FMR vs input rf power, repetition rate 7.3 kHz. The temperature set point is raised to 87 K so that the effective sample temperature lies close to that of the 75 K experiments taken at 252 kHz (Figs. 3–5).

IV. MODEL AND DISCUSSION

We now discuss the origins of these nonlinearities. In a first approach we describe analytically the system as a forced parametric oscillator [12,36]. We then compare it to a full numerical solution of the Landau-Lifshitz-Gilbert equation in the presence of SAW. In both cases we use the free-energy form for (Ga,Mn)As [30] and the standard magnetoelastic energy of a cubic system as given in Appendix A.

The LLG equation is first linearized with respect to the magnetization oscillating components ($\delta\theta$, $\delta\phi$), thus ignoring intrinsic magnetic nonlinearities but keeping those arising from the SAW driving. This leads to a linear parametric equations system [Eqs. (1) and (2)],

$$\ddot{\delta\theta} + 2(\Gamma_0 + \Gamma_1\epsilon_{XX})\dot{\delta\theta} + \delta\theta\left(\Omega_0^2 + \Omega_1^2\epsilon_{XX}\right) + C_\theta\dot{\epsilon}_{XX}\delta\phi = F_{1\theta}\omega_{saw}^{-1}\dot{\epsilon}_{XX}, \tag{1}$$

$$\ddot{\delta\phi} + 2(\Gamma_0 + \Gamma_1\epsilon_{XX})\dot{\delta\phi} + \delta\phi\left(\Omega_0^2 + \Omega_1^2\epsilon_{XX}\right) + C_\phi\dot{\epsilon}_{XX}\delta\theta = F_{1\phi}\epsilon_{XX} + F_{2\phi}\epsilon_{XX}^2, \tag{2}$$

where Γ_0 and Ω_0 are the damping and angular frequency of the free ($\delta\theta$, $\delta\phi$) oscillators, respectively. For the sake of clarity only $\epsilon_{XX} = \epsilon_{XX0}\sin(\omega_{saw}t - k_{saw}X)$ is kept here. Its contribution is anyway found to be dominant. The linear regime results from the driving forces linear in ϵ_{XX} ($F_{1\theta}$ and $F_{1\phi}$ terms). Nonlinearities arise from the products $\epsilon_{XX}\delta\theta$, $\epsilon_{XX}\delta\phi$ in the parametric damping (Γ_1), frequency (Ω_1), and coupling (C_θ, C_ϕ) terms and from the $F_{2\phi}\epsilon_{XX}^2$ driving term. These nonlinear terms depend on B_1 and B_2 magnetoelastic constants, and on the static magnetization position (see Appendix A). In a perturbative approach the solutions are obtained as the sum of two terms, oscillating at $f_{saw} = \omega_{saw}/2\pi$ and $2f_{saw}$ and a SAW-dependent offset (constant term), as obtained experimentally (Figs. 3, 5, and 6). The $\delta\theta$ amplitudes at f_{saw} and $2f_{saw}$ are given by Eqs. (3) and (4) (the other amplitudes can be found in Appendix A),

$$\delta\theta_{f_{saw}}(B,t,X) = \epsilon_{XX0}\frac{|F_{1\theta}|}{\sqrt{(\Omega_0^2 - \omega_{saw}^2)^2 + 4\Gamma_0^2\omega_{saw}^2}}\sin[\omega_{saw}t - k_{saw}X + \psi_1(B)], \tag{3}$$

$$\delta\theta_{2f_{saw}}(B,t,X) = \epsilon_{XX0}^2\frac{\left|\Omega_1^2F_{1\theta} + C_\theta\omega_{saw}F_{1\phi}\right|}{2\sqrt{(\Omega_0^2 - \omega_{saw}^2)^2 + 4\Gamma_0^2\omega_{saw}^2}\sqrt{(\Omega_0^2 - 4\omega_{saw}^2)^2 + 16\Gamma_0^2\omega_{saw}^2}}\sin[2\omega_{saw}t - 2k_{saw}X + \psi_2(B)], \tag{4}$$

where $\psi_{(1,2)}(B)$ are the phase shifts with respect to the SAW. The two important contributions to $\delta\theta_{2f_{saw}}$ are the parametric frequency (Ω_1) and coupling (C_θ) terms that are found to have similar weights.

A linearized form of LLG with parametric coupling is thus enough to generate frequency doubling (both in time and in space) without invoking magnetic nonlinear interactions, as already highlighted in Ref. [12]. Since the driving forces

$F_{1\theta}$ and $F_{1\phi}$ are proportional to $B_2 \sin 2\phi_0$, both $\delta\theta_{f_{saw}}$ and $\delta\theta_{2f_{saw}}$ amplitudes cancel out for the magnetization parallel or perpendicular to $\mathbf{k}_{saw}$ ($\phi_0 = 0$ or $\frac{\pi}{2}$). The f_{saw} term resonates when $\Omega_0(B) = \omega_{saw}$. One moreover sees that it is the B_2 magnetoelastic component that drives the precession. The $2f_{saw}$ term resonates at fields such that $\Omega_0(B) = \omega_{saw}$ and $2\omega_{saw}$. In our case, these two resonance fields are always close enough for the two resonances to merge into a broad one (the damping will of course encourage this as well). These resonances are well observed experimentally, at either $T = 42$ or 75 K (Fig. 3). What ensures efficient concomitant f and $2f$ excitation is the coexistence of their resonance conditions for close enough fields. This is made possible by a $\Omega_0(B)$ curve exhibiting a sufficiently steep slope. As appears in Figs. 3(g) and 3(h), in our system this happens close to saturation indeed ($T = 42$ and 75 K), or far from it (unlike the case of Ref. [18]), at very low field in the case of competing uniaxial and biaxial anisotropies ($T = 75$ K only).

We now discuss the evolution of the precession amplitude with the drive field. In the perturbative approach, the amplitude of the f_{saw} ($2f_{saw}$) term is expected to be linear (quadratic) with SAW amplitude, without any thresholding effect for the appearance of $2f_{saw}$ [Eqs. (3) and (4)]. This is indeed what we observe, up to a certain SAW amplitude (corresponding to $A_{GaAs} \approx 7$ μrad in Fig. 5). At the maximum SAW amplitude (plateau of the acoustic pulse, $\Delta\tau = 3.52$ μs), the amplitude of $2f_{saw}$ still follows a smooth quadratic evolution while the evolution of the f_{saw} term tails off, a clear indication of sublinear magnetic susceptibility, which requires genuine nonlinear interaction terms in the LLG equation. The sublinear evolution of the f_{saw} amplitude cannot be rendered within a perturbation approach. It can, however, easily be reproduced when doing a full numerical resolution of the magnetoacoustic dynamics as shown in Fig. 5(c). Comparing the two approaches highlights that, contrary to what is commonly accepted, a linearized description of the dynamics ceases to be valid even for quite small precession amplitudes, e.g., a few mrad ($\approx 0.1^\circ$) for $\delta\theta$.

The $\delta\theta$ and $\delta\phi$ precession amplitudes at f_{saw} and $2f_{saw}$ were calculated as a function of the applied magnetic field, using either the analytical solutions from the parametric oscillator model or the full LLG numerical solutions [Figs. 3(e) and 3(f)]. $\delta\theta$ and $\delta\phi$ differ in amplitude but have a similar field dependence, therefore we show only the $\delta\theta$ curves. The experimental results showing one broad field resonance at 42 K and two resonances at 75 K are well reproduced using the parametric oscillator model. It is worth noting that the calculated $\delta\theta$ amplitudes are reasonably consistent with the experimental Kerr signal $\mathcal{K}\delta\theta$ since the Kerr coefficient $\mathcal{K}$ is of the order of 5–10 mrad in (Ga,Mn)As [35]. These $\delta\theta$ amplitudes are obtained using a SAW strain amplitude $\epsilon_{XX0} = 2 \times 10^{-5}$, fully consistent with the experimental determination of the SAW strain for similar rf powers [40]. However, the perturbative approach overestimates the precession amplitudes, all the more as the SAW amplitude increases, as seen in Fig. 5(c).

The $\delta\theta$ amplitudes obtained using the full LLG equations are very close to the ones from the parametric oscillator model at 75 K [Fig. 3(f)]. At 42 K [Fig. 3(e)] they differ in two ways: (i) The peak of the f_{saw} component slightly shifts to a lower field, and (ii) a dip appears in the $2f_{saw}$ amplitude. These changes can be traced to the contribution of quadratic terms $\delta\theta^2$, $\delta\phi^2$, and $\delta\theta\delta\phi$. For a given SAW amplitude the importance of these intrinsic nonlinearities depends on temperature via the magnetization, and the cubic and uniaxial in-plane magnetic anisotropy constants.

We conclude that, while the parametric oscillator model, including only SAW-induced nonlinearities, accounts for the time and space frequency doubling of the magnetization dynamics, the full LLG model, including also magnetic nonlinear terms, is necessary to capture the dependence of magnetization dynamics on the SAW amplitude and the shift of the resonance.

V. CONCLUSION

Clear frequency and wave-vector doubling have been observed under surface-acoustic-wave-driven magnetization precession. Several other features of nonlinear magnetic dynamics have been evidenced, such as the downshift of the resonance field and the quadratic evolution of the double-frequency term. This approach has the advantage of not requiring any power threshold for the appearance of extra frequencies, contrary to parametric pumping which relies on Suhl instabilities. The efficient cogeneration of both f_{saw} and $2f_{saw}$ terms mainly depends on the shape of the $f_{prec}(B)$ curve and the proximity of f and $2f$ resonance fields. While the demonstration of this effect was made particularly easy in (Ga,Mn)As with its temperature-variable f_{prec} curve and large magneto-optical coefficients, it should be possible to obtain similar results in room-temperature ferromagnets. Numerous applications can be imagined for this effect, such as the implementation of SAWs in neuromorphic computing [41], for which nonlinearities are a prerequisite, or the design of nonreciprocal magnonic crystals.

ACKNOWLEDGMENTS

We acknowledge financial support from the French Ministry of Foreign Affairs through the project PHC Utique 16G1303. We are grateful to H. J. von Bardeleben (INSP) for providing the cavity FMR data, and to M. Bernard, M. Vabre, F. Breton, and S. Majrab (INSP) for technical assistance.

APPENDIX A: PARAMETRIC OSCILLATOR

In order to obtain the parametric oscillator equations, we start from the Landau-Lifschitz-Gilbert (LLG) in the linearized form for a system with magnetization M in a macrospin approach (exchange neglected [33]),

$$\dot{\delta\theta} + \alpha\dot{\delta\phi} + \left(\omega_{\phi\phi} + \omega_{\phi\phi}^{saw}\right)\delta\phi + \omega_{\theta\phi}^{saw}\delta\theta + \omega_{\phi}^{saw} = 0,$$
$$\dot{\delta\phi} - \alpha\dot{\delta\theta} - \left(\omega_{\theta\theta} + \omega_{\theta\theta}^{saw}\right)\delta\theta - \omega_{\theta\phi}^{saw}\delta\phi - \omega_{\theta}^{saw} = 0,$$

where $\delta\theta$ and $\delta\phi$ are the small deviations of the magnetization unit vector from the equilibrium position given by the polar angle $\theta_0 = \pi/2$ and the azimuthal angle ϕ_0 and the dot denotes the time derivative. α is the Gilbert damping. We define $\omega_{ij} = \gamma \frac{\partial^2 F}{\partial i \partial j}$, where (i, j) refer to the θ and ϕ variables and $MF = E_m$ is the magnetic energy including the Zeeman energy, the shape magnetic anisotropy energy, and

the magnetocrystalline anisotropy energy, which contains the magnetoelastic part arising from epitaxial strain [30].

$$E_m = -K_{2\perp}\cos^2\theta - K_{2\parallel}\sin^2\theta\sin^2\left(\phi-\frac{\pi}{4}\right) - \frac{K_{4\parallel}}{8}(3+\cos 4\phi)\sin^4\theta - \frac{K_{4\perp}}{2}\cos^4\theta - \frac{\mu_0}{2}M^2\sin^2\theta.$$

Similarly we define $\omega_{ij}^{\rm saw} = \gamma\frac{\partial^2 F_{\rm mel}^{\rm saw}}{\partial i\,\partial j}$, $\omega_i^{\rm saw} = \gamma\frac{\partial F_{\rm mel}^{\rm saw}}{\partial i}$, where $MF_{\rm mel}^{\rm saw}$ is the part of the magnetoelastic energy related to the dynamic strain imposed by the SAW. Since the epitaxial tetragonal strain is very weak, we use the usual expression for cubic symmetry for $F_{\rm mel}$,

$$F_{\rm mel} = \frac{B_1}{M}\left(m_x^2\epsilon_{xx} + m_y^2\epsilon_{yy} + m_z^2\epsilon_{zz}\right) + 2\frac{B_2}{M}(m_x m_y\epsilon_{xy} + m_x m_z\epsilon_{xz} + m_y m_z\epsilon_{yz}), \quad \text{(A1)}$$

where (x, y, z) are the coordinates related to the $\langle 100\rangle$ cubic axes. Parameters B_1 and B_2 are obtained from the magnetic anisotropy constants in Eq. (A1) and the static epitaxial strain $B_1 = -\frac{K_{2\perp}-K_{2\parallel}/2}{\epsilon_{zz}^0-\frac{\epsilon_{xx}^0+\epsilon_{yy}^0}{2}}$, $B_2 = \frac{K_{2\parallel}}{2\epsilon_{xy}^0}$, where the ϵ_{ii}^0 are the static epitaxial strain components and $\epsilon_{xy}^0 = 10^{-4}$ is the effective shear strain necessary to account for the in-plane unixial magnetic anisotropy ($K_{2\parallel}$) [42,43].

From the equations above we obtain the system of two coupled parametric oscillators where we only keep terms that will give oscillations of the magnetization vector at $f_{\rm saw}$ and $2f_{\rm saw}$ in the forced regime,

$$\ddot{\delta\theta} + 2\left(\Gamma_0+\Gamma_{1\epsilon}\right)\dot{\delta\theta} + \delta\theta\left(\Omega_0^2+\Omega_{1\epsilon}^2+\Omega_{1\epsilon\theta}^2\right) + C_{1\epsilon\theta}\delta\phi = F_{1\epsilon\theta} + F_{2\epsilon\theta}, \quad \text{(A2)}$$

$$\ddot{\delta\phi} + 2\left(\Gamma_0+\Gamma_{1\epsilon}\right)\dot{\delta\phi} + \delta\phi\left(\Omega_0^2+\Omega_{1\epsilon}^2+\Omega_{1\epsilon\phi}^2\right) + C_{1\epsilon\phi}\delta\theta = F_{1\epsilon\phi} + F_{2\epsilon\phi}, \quad \text{(A3)}$$

where $\Gamma_0 = \frac{\alpha(\omega_{\theta\theta}+\omega_{\phi\phi})}{2(1+\alpha^2)}$ and $\Omega_0^2 = \frac{\omega_{\theta\theta}\omega_{\phi\phi}}{(1+\alpha^2)}$ are the damping and angular eigenfrequency of the free oscillators, respectively. The damping (Γ), frequency (Ω), coupling parameter (C), and driving force (F) with index ϵ depend on the SAW strain tensor components. They are expressed as

$$\Gamma_{1\epsilon} = \frac{\alpha}{2}\left(\omega_{\theta\theta}^{\rm saw}+\omega_{\phi\phi}^{\rm saw}\right), \quad \text{(A4)}$$

$$\Omega_{1\epsilon}^2 = \omega_{\phi\phi}\omega_{\theta\theta}^{\rm saw} + \omega_{\theta\theta}\omega_{\phi\phi}^{\rm saw}, \quad \text{(A5)}$$

$$\Omega_{1\epsilon\theta}^2 = \alpha\dot{\omega}_{\theta\theta}^{\rm saw} + \dot{\omega}_{\theta\phi}^{\rm saw}, \quad \Omega_{1\epsilon\phi}^2 = \alpha\dot{\omega}_{\phi\phi}^{\rm saw} - \dot{\omega}_{\theta\phi}^{\rm saw}, \quad \text{(A6)}$$

$$C_{1\epsilon\theta} = \dot{\omega}_{\phi\phi}^{\rm saw} + \alpha\dot{\omega}_{\theta\phi}^{\rm saw}, \quad C_{1\epsilon\phi} = -\dot{\omega}_{\theta\theta}^{\rm saw} + \alpha\dot{\omega}_{\theta\phi}^{\rm saw}, \quad \text{(A7)}$$

$$F_{1\epsilon\theta} = -\left(\alpha\dot{\omega}_{\theta}^{\rm saw} + \dot{\omega}_{\phi}^{\rm saw} + \omega_{\theta}^{\rm saw}\omega_{\phi\phi}\right), \quad \text{(A8)}$$

$$F_{2\epsilon\theta} = \omega_{\theta\phi}^{\rm saw}\omega_{\phi}^{\rm saw} - \omega_{\theta}^{\rm saw}\omega_{\phi\phi}^{\rm saw}, \quad \text{(A9)}$$

$$F_{1\epsilon\phi} = \dot{\omega}_{\theta}^{\rm saw} - \alpha\dot{\omega}_{\phi}^{\rm saw} - \omega_{\phi}^{\rm saw}\omega_{\theta\theta}, \quad \text{(A10)}$$

$$F_{2\epsilon\phi} = \omega_{\theta\phi}^{\rm saw}\omega_{\theta}^{\rm saw} - \omega_{\phi}^{\rm saw}\omega_{\theta\theta}^{\rm saw}. \quad \text{(A11)}$$

Note that since $\alpha \ll 1$ in (Ga,Mn)As, the approximation $(1+\alpha^2)\approx 1$ has been used in the calculations.

A SAW propagating along [-110] has strain components $\epsilon_{\rm XX}$, $\epsilon_{\rm ZZ}$, and $\epsilon_{\rm XZ}$. Since the latter two are found to give a negligible contribution to the magnetization dynamics in our sample, we will neglect them hereafter. The equations of the coupled parametric oscillators then read

$$\ddot{\delta\theta} + 2\left(\Gamma_0+\Gamma_1\epsilon_{\rm XX}\right)\dot{\delta\theta} + \delta\theta\left(\Omega_0^2+\Omega_1^2\epsilon_{\rm XX}\right) + C_\theta\dot{\epsilon}_{\rm XX}\delta\phi = F_{1\theta}\omega_{\rm saw}^{-1}\dot{\epsilon}_{\rm XX}, \quad \text{(A12)}$$

$$\ddot{\delta\phi} + 2(\Gamma_0+\Gamma_1\epsilon_{\rm XX})\dot{\delta\phi} + \delta\phi\left(\Omega_0^2+\Omega_1^2\epsilon_{\rm XX}\right) + C_\phi\dot{\epsilon}_{\rm XX}\delta\theta = F_{1\phi}\epsilon_{\rm XX} + F_{2\phi}\epsilon_{\rm XX}^2, \quad \text{(A13)}$$

where $\epsilon_{\rm XX}$ stands for $\epsilon_{\rm XX0}\sin(\omega_{\rm saw}t - k_{\rm saw}X)$. The strain amplitude $\epsilon_{\rm XX0}$ is taken at $Z=0$ since the thickness of the magnetic layer (45 nm) is much smaller than the SAW penetration depth (a few μm). In the damping, frequency, coupling parameters, and driving forces, we have kept only the leading terms in powers of α. Note that the coupling terms C_θ, C_ϕ contribute only to the amplitudes at $2f_{\rm saw}$. The parameters read

$$\Gamma_1 = -\frac{\alpha}{2}(\omega_1 + 3\omega_2\cos 2\phi_0), \quad \text{(A14)}$$

$$\Omega_1^2 = -\omega_2\cos 2\phi_0(2\omega_{\theta\theta}+\omega_{\phi\phi}) - \omega_1\omega_{\phi\phi}, \quad \text{(A15)}$$

$$C_\theta = -2\omega_2\cos 2\phi_0, \quad \text{(A16)}$$

$$C_\phi = (\omega_1 + \omega_2\cos 2\phi_0), \quad \text{(A17)}$$

$$F_{1\theta} = \omega_2\omega_{\rm saw}\sin 2\phi_0, \quad \text{(A18)}$$

$$F_{1\phi} = \omega_2\omega_{\theta\theta}\sin 2\phi_0, \quad \text{(A19)}$$

$$F_{2\phi} = -\omega_2(\omega_1 + \omega_2\cos 2\phi_0)\sin 2\phi_0, \quad \text{(A20)}$$

where $\omega_1 = \gamma B_1/M$, $\omega_2 = \gamma B_2/M$, with γ the gyromagnetic factor, and $\omega_{\theta\theta}, \omega_{\phi\phi}$ depend on ϕ_0.

Let us note that the driving forces are proportional to $\sin(2\phi_0)$ and hence vanish when the magnetization is aligned with the [-110] direction (at zero field) or perpendicular to it (at fields larger than H_a).

Solving perturbatively Eqs. (A12) and (A13), the $\delta\theta$ and $\delta\phi$ amplitudes at frequencies $f_{\rm saw}$ and $2f_{\rm saw}$ are

$$\delta\theta_{f_{\rm saw}} = \epsilon_{\rm XX0}\frac{|F_{1\theta}|}{\sqrt{\left({\Omega_0}^2-\omega_{\rm saw}^2\right)^2+4\Gamma_0^2\omega_{\rm saw}^2}}, \tag{A21}$$

$$\delta\phi_{f_{\rm saw}} = \epsilon_{\rm XX0}\frac{|F_{1\phi}|}{\sqrt{\left({\Omega_0}^2-\omega_{\rm saw}^2\right)^2+4\Gamma_0^2\omega_{\rm saw}^2}}, \tag{A22}$$

$$\delta\theta_{2f_{\rm saw}} = \epsilon_{\rm XX0}^2\frac{\left|\Omega_1^2F_{1\theta}+C_\theta\omega_{\rm saw}F_{1\phi}\right|}{2\sqrt{\left({\Omega_0}^2-\omega_{\rm saw}^2\right)^2+4\Gamma_0^2\omega_{\rm saw}^2}\sqrt{\left(\Omega_0^2-4\omega_{\rm saw}^2\right)^2+16\Gamma_0^2\omega_{\rm saw}^2}}, \tag{A23}$$

$$\delta\phi_{2f_{\rm saw}} = \epsilon_{\rm XX0}^2\frac{\left|\Omega_1^2F_{1\phi}-C_\phi\omega_{\rm saw}F_{1\theta}-F_{2\phi}\left(\Omega_0^2-\omega_{\rm saw}^2\right)\right|}{2\sqrt{\left({\Omega_0}^2-\omega_{\rm saw}^2\right)^2+4\Gamma_0^2\omega_{\rm saw}^2}\sqrt{\left(\Omega_0^2-4\omega_{\rm saw}^2\right)^2+16\Gamma_0^2\omega_{\rm saw}^2}}. \tag{A24}$$

For $\delta\theta_{2f_{\rm saw}}$, it is found numerically that the parametric frequency (Ω_1) and coupling (C_θ) terms give equal contributions. For $\delta\phi_{2f_{\rm saw}}$ the dominant contribution is the parametric frequency term $\Omega_1^2F_{1\phi}$. Similarly to the driving forces, the precession amplitudes are proportional to $\omega_2\sin 2\phi_0$.

A perturbation at $\omega_{\rm saw}$ not only provides a signal at $\omega_{\rm saw}+\omega_{\rm saw}=2\omega_{\rm saw}$ but also at $(\omega_{\rm saw}-\omega_{\rm saw}=0)$, i.e., frequency-independent offsets $\delta\theta_0$ and $\delta\phi_0$. They are both proportional to the square of the SAW amplitude and have a significant amplitude only close to $\Omega_0=\omega_{\rm saw}$. $\delta\theta_0$ is proportional to the damping α, hence much smaller than $\delta\phi_0$, as observed experimentally (Fig. 6). It is worth noting that these constant terms are missed when working with complex amplitudes instead of real ones as in Ref. [12], as well as the factor 2 in the amplitudes $\delta\theta_{2f_{\rm saw}}$ and $\delta\phi_{2f_{\rm saw}}$ [Eqs. (A23) and (A24)].

When keeping all the SAW strain components, the driving forces in Eqs. (A2) and (A3) become

$$F_{1\epsilon\theta} = \omega_2(\sin(2\phi_0)\dot{\epsilon}_{\rm XX}+2\alpha\cos(\phi_0)\dot{\epsilon}_{\rm XZ} +2\cos(\phi_0)\omega_{\phi\phi}(\phi_0)\epsilon_{\rm XZ}), \tag{A25}$$

$$F_{2\epsilon\theta} = -4\omega_2^2\cos(\phi_0)^3\epsilon_{\rm XX}\epsilon_{\rm XZ}, \tag{A26}$$

$$F_{1\epsilon\phi} = \omega_2(\alpha\sin(2\phi_0)\dot{\epsilon}_{\rm XX}-2\cos(\phi_0)\dot{\epsilon}_{\rm XZ}\omega_{\theta\theta}(\phi_0) \times\sin(2\phi_0)\epsilon_{\rm XX}), \tag{A27}$$

$$F_{2\epsilon\phi} = -\omega_2\sin(2\phi_0)\big((\omega_1(\epsilon_{\rm XX}-2\epsilon_{\rm ZZ}) +\omega_2\cos(2\phi_0)\epsilon_{\rm XX})\epsilon_{\rm XX}+2\omega_2\epsilon_{\rm XZ}^2\big). \tag{A28}$$

When $\sin 2\phi_0$ becomes zero (magnetization aligned along $\mathbf{k}_{\rm saw}$ or along a saturating field parallel to the [110] direction), the driving forces arise solely from the (weak) $\epsilon_{\rm XZ}$ strain component owing to the $\cos(\phi_0)$ factor, which is nonzero only if the magnetization is aligned with $\mathbf{k}_{\rm saw}$ ($\phi_0=0$). The $\epsilon_{\rm ZZ}$ strain component is seen to appear via the B_1 magnetoelastic coefficient, and only in the double-frequency term. $\epsilon_{\rm ZZ}$ at the surface is smaller than $\epsilon_{\rm XX}$: From the solutions of the Rayleigh wave propagation equations we obtain $\epsilon_{\rm ZZ0}=-0.34\epsilon_{\rm XX0}$.

The parameters used for the numerical calculations are as follows. For the $T=42$ K data, $K_{2\perp}=-5.9$ kJ m^{-3}, $K_{2\parallel}=0.4$ kJ m^{-3}, $K_{4\parallel}=K_{4\perp}=90$ J m^{-3}, $M=39$ kA m^{-1}, $\frac{B_1}{M}=40.7$ T, $\frac{B_2}{M}=53$ T. For the $T=75$ K data, $K_{2\perp}=-3.65$ kJ m^{-3}, $K_{2\parallel}=45$ J m^{-3}, $K_{4\parallel}=K_{4\perp}=43$ J m^{-3}, $M=20$ kA m^{-1}, $\frac{B_1}{M}=47.7$ T, $\frac{B_2}{M}=11.2$ T. For all simulations, the field was misaligned by 0.5° from the [110] direction to render more realistic resonance curves, $\alpha=0.05$ and $\epsilon_{\rm XX0}=2.5\times10^{-5}$.

APPENDIX B: rf EXCITATION-INDUCED TEMPERATURE RISE

The combination of a high instantaneous rf power (+28 dBm and above), 10% duty cycle, and a poor impedance match between the IDTs and the rf source results in a sizable stationary temperature rise. Since the magnetic parameters, in particular, the resonance frequency, resonance fields, and resulting precession amplitude, are very sensitive to temperature in (Ga,Mn)As, one must take this into account when studying the effect of SAW amplitude. With this in mind, two strategies were therefore adopted in this work: (i) working at a high repetition rate (252 kHz) and constant rf input power, and exploiting the varying SAW amplitude during the rise time of the acoustic burst by playing on the delay between the rf burst and laser pulses (Fig. 5), and (ii) working at a much lower repetition rate (7.3 kHz instead of 252 kHz) and varying the rf input power (Fig. 7). This was implemented when only electrical data were needed, since the signal-to-noise ratio of the optical time-domain data becomes prohibitively bad for laser repetition rates below 100 kHz.

The stationary temperature rise induced by the pulsed rf excitation was nevertheless estimated as follows, using the Rayleigh-wave velocity as a sensitive probe of the relative temperature changes. Acoustic velocity variations dV/V were measured electrically following the procedure described in Refs. [5,26], after two different modifications of the effective sample temperature: (i) Working at a constant 2.5 kHz laser repetition rate and $P_{\rm rf}=+21$ dBm, the cryostat temperature set point was changed abruptly from $T_0=77$ K to $T_0+\delta T$. This resulted in a gradual change of the acoustic phase, and the final dV/V was measured once the stationary regime was reached. δT was varied between 1 and 20 K. (ii) Working at a constant $T_0=77$ K, and abruptly changing the laser

repetition rate from 2.5 to 252 kHz. This was done for P_{rf} ranging from +5 to +31 dBm. We then compared the measured phase (velocity) changes when varying either δT or P_{rf} and obtained an experimental $\delta T(P_{\mathrm{rf}})$ abacus. The stationary temperature rise in the experimental conditions of Figs. 3–5 was thus estimated to around 12 ± 2 K. It is naturally intimately related to the rf burst duration and periodicity, and equivalent electrical circuit, so this value should not be taken out of the context of this experiment. It was shown to depend very weakly on the rf frequency, however, confirming that the heating is not primarily of thermoelastic origin.

[1] T. Gerrits, P. Krivosik, M. L. Schneider, C. E. Patton, and T. J. Silva, Phys. Rev. Lett. **98**, 207602 (2007).

[2] V. E. Demidov, M. P. Kostylev, K. Rott, P. Krzysteczko, G. Reiss, and S. O. Demokritov, Phys. Rev. B **83**, 054408 (2011).

[3] A. G. Gurevich and G. A. Melkov, *Magnetization Oscillations and Waves* (CRC Press, New York, 1996).

[4] Y. Shiota, T. Nozaki, F. Bonell, S. Murakami, T. Shinjo, and Y. Suzuki, Nat. Mater. **11**, 39 (2012).

[5] L. Thevenard, I. S. Camara, S. Majrab, M. Bernard, P. Rovillain, A. Lemaître, C. Gourdon, and J.-Y. Duquesne, Phys. Rev. B **93**, 134430 (2016).

[6] A. N. Slavin and V. Tiberkevich, IEEE Trans. Magn. **45**, 1875 (2009).

[7] J. Torrejon, M. Riou, F. A. Araujo, S. Tsunegi, G. Khalsa, D. Querlioz, P. Bortolotti, V. Cros, A. Fukushima, H. Kubota, S. Yuasa, M. D. Stiles, and J. Grollier, Nature (London) **547**, 428 (2017).

[8] T. Brächer and P. Pirro, J. Appl. Phys. **124**, 152119 (2018).

[9] A. A. Serga, A. V. Chumak, and B. Hillebrands, J. Phys. D: Appl. Phys. **43**, 264002 (2010).

[10] A. V. Chumak, A. A. Serga, and B. Hillebrands, Nat. Commun. **5**, 4700 (2014).

[11] Q. Wang, M. Kewenig, M. Schneider, R. Verba, B. Heinz, M. Geilen, M. Mohseni, B. Lägel, F. Ciubotaru, C. Adelmann, C. Dubs, S. D. Cotofana, T. Brächer, P. Pirro, and A. V. Chumak, arXiv:1905.12353.

[12] C. L. Chang, A. M. Lomonosov, J. Janusonis, V. S. Vlasov, V. V. Temnov, and R. I. Tobey, Phys. Rev. B **95**, 060409(R) (2017).

[13] M. Foerster, F. Macià, N. Statuto, S. Finizio, A. Hernández-Mínguez, S. Lendínez, P. V. Santos, J. Fontcuberta, J. M. Hernàndez, M. Kläui, and L. Aballe, Nat. Commun. **8**, 407 (2017).

[14] P. Kuszewski, J.-Y. Duquesne, L. Becerra, A. Lemaître, S. Vincent, S. Majrab, F. Margaillan, C. Gourdon, and L. Thevenard, Phys. Rev. Appl. **10**, 034036 (2018).

[15] A. S. Salasyuk, A. V. Rudkovskaya, A. P. Danilov, B. A. Glavin, S. M. Kukhtaruk, M. Wang, A. W. Rushforth, P. A. Nekludova, S. V. Sokolov, A. A. Elistratov, D. R. Yakovlev, M. Bayer, A. V. Akimov, and A. V. Scherbakov, Phys. Rev. B **97**, 060404(R) (2018).

[16] M. Weiler, H. Huebl, F. S. Goerg, F. D. Czeschka, R. Gross, and S. T. B. Goennenwein, Phys. Rev. Lett. **108**, 176601 (2012).

[17] P. G. Gowtham, D. Labanowski, and S. Salahuddin, Phys. Rev. B **94**, 014436 (2016).

[18] A. Capua, C. Rettner, and S. S. P. Parkin, Phys. Rev. Lett. **116**, 047204 (2016).

[19] C. Cheng and W. E. Bailey, Appl. Phys. Lett. **103**, 242402 (2013).

[20] P. Chowdhury, A. Jander, and P. Dhagat, IEEE Magn. Lett. **8**, 3108204 (2017).

[21] H. Keshtgar, M. Zareyan, and H. G. Bauer, Solid State Commun. **198**, 30 (2014).

[22] H. Matthews and F. R. Morgenthaler, Phys. Rev. Lett. **13**, 614 (1964).

[23] N. Tiercelin, A. Talbi, S. Giordano, A. Klimov, T. Mathurin, O. Elmazria, M. Hehn, V. Preobrazhensky, O. Bou Matar, Y. Dusch, and P. Pernod, in *Spintronics X*, edited by H. Jaffrès, H.-J. Drouhin, J.-E. Wegrowe, and M. Razeghi (SPIE, Bellingham, WA, 2017), p. 64.

[24] I. Lisenkov, A. Jander, and P. Dhagat, Phys. Rev. B **99**, 184433 (2019).

[25] P. Delsing, A. N. Cleland, M. J. A. Schuetz, J. Knörzer, G. Giedke, J. I. Cirac, K. Srinivasan, M. Wu, K. C. Balram, C. Bäuerle, T. Meunier, C. J. B. Ford, P. V. Santos, E. Cerda-Méndez, H. Wang, H. J. Krenner, E. D. S. Nysten, M. Weiß, G. R. Nash, L. Thevenard *et al.*, J. Phys. D: Appl. Phys. **52**, 353001 (2019).

[26] J.-Y. Duquesne, P. Rovillain, C. Hepburn, M. Eddrief, P. Atkinson, A. Anane, R. Ranchal, and M. Marangolo, Phys. Rev. Applied **12**, 024042 (2019).

[27] S. Davis, J. A. Borchers, B. B. Maranville, and S. Adenwalla, J. Appl. Phys. **117**, 063904 (2015).

[28] K. An, A. N. Litvinenko, A. A. Fuad, V. V. Naletov, L. Vila, U. Ebels, G. de Loubens, H. Hurdequint, N. Beaulieu, J. B. Youssef, N. Vukadinovic, G. E. W. Bauer, A. N. Slavin, V. S. Tiberkevich, and O. Klein, Phys. Rev. B **101**, 060407 (2020).

[29] A. Lemaître, A. Miard, L. Travers, O. Mauguin, L. Largeau, C. Gourdon, V. Jeudy, M. Tran, and J.-M. George, Appl. Phys. Lett. **93**, 21123 (2008).

[30] L. Thevenard, J.-Y. Duquesne, E. Peronne, H. J. von Bardeleben, H. Jaffrès, S. Ruttala, J.-M. George, A. Lemaître, and C. Gourdon, Phys. Rev. B **87**, 144402 (2013).

[31] P. Kuszewski, I. S. Camara, N. Biarrotte, L. Becerra, J. von Bardeleben, W. Savero Torres, A. Lemaître, C. Gourdon, J.-Y. Duquesne, and L. Thevenard, J. Phys.: Condens. Matter **30**, 244003 (2018).

[32] F. J. R. Schülein, E. Zallo, P. Atkinson, O. G. Schmidt, R. Trotta, A. Rastelli, A. Wixforth, and H. J. Krenner, Nat. Nanotechnol. **10**, 512 (2015).

[33] Spin waves excited at f_{saw} and k_{saw} have almost zero group velocity, hence there are no interferences of spin waves excited at different locations .

[34] P. Chowdhury, P. Dhagat, and A. Jander, IEEE Trans. Magn. **51**, 1 (2015).

[35] S. Shihab, L. Thevenard, A. Lemaître, and C. Gourdon, Phys. Rev. B **95**, 144411 (2017).

[36] H. G. Bauer, P. Majchrak, T. Kachel, C. H. Back, and G. Woltersdorf, Nat. Commun. **6**, 8274 (2015).

[37] D. J. Seagle, S. H. Charap, and J. O. Artman, J. Appl. Phys. **57**, 3706 (1985).

[38] W. Chen, G. De Loubens, J.-M. L. Beaujour, J. Z. Sun, and A. D. Kent, Appl. Phys. Lett. **95**, 172513 (2009).
[39] R. Inaba and N. Mikoshiba, Appl. Phys. Lett. **41**, 25 (1982).
[40] L. Largeau, I. S. Camara, J.-Y. Duquesne, C. Gourdon, P. Rovillain, L. Thevenard, and B. Croset, J. Appl. Crystallogr. **49**, 2073 (2016).
[41] Y. Katayama, T. Yamane, D. Nakano, R. Nakane, and G. Tanaka, IEEE Trans. Nanotechnol. **15**, 762 (2016).
[42] J. Zemen, J. Kučera, K. Olejník, and T. Jungwirth, Phys. Rev. B **80**, 155203 (2009).
[43] M. Kraimia, L. Largeau, K. Boujdaria, B. Croset, C. Mocuta, and A. Lemaître, J. Appl. Phys. **127**, 093901 (2020).